Empirical Removal of Tides and Inverse Barometer Effect on DInSAR From Double DInSAR and a Regional Climate Model

Quentin Glaude, *Graduate Student Member, IEEE*, Charles Amory, Sophie Berger, Dominique Derauw, Frank Pattyn, Christian Barbier, and Anne Orban

***Abstract*—Ice shelves—the floating extensions of the Antarctic ice sheet—regulate the Antarctic contribution to sea-level rise by restraining the grounded ice flowing from upstream. Therefore, ice-shelf change (e.g., ice-shelf thinning) results in accelerated ice discharge into the ocean, which has a direct effect on sea level. Studying ice-shelf velocity allows the monitoring of the ice shelves' stability and evolution. Differential synthetic aperture radar interferometry (DInSAR) is a common technique from which highly accurate velocity maps can be inferred at high resolution. Because ice shelves are afloat, small sea-level changes—i.e., ocean tides and varying atmospheric pressure (aka inverse barometer effect) lead to vertical displacements. If not accounted for in the interferometric process, these effects will induce a strong bias in the horizontal velocity estimation. In this article, we present an empirical DInSAR correction technique from geophysical models and double DInSAR, with a study on its variance propagation. The method is developed to be used at large coverage on short timescales, essential for the near-continuous monitoring of rapidly changing areas on polar ice sheets. We used Sentinel-1 SAR acquisitions in interferometric wide and extra -wide swath modes. The vertical interferometric bias is estimated using a regional climate model (MAR) and a tide model (CATS2008). The study area is located on the Roi Baudouin Ice Shelf in Dronning Maud Land, East Antarctica. Results show a major decrease (67 m·a^{-1}) in the vertical-induced displacement bias.**

***Index Terms*—Antarctica, differential synthetic aperture radar (SAR) interferometry (DInSAR), double DInSAR (DDInSAR), ice shelf, inverse barometer effect (IBE), tides.**

I. Introduction

THINNING of Antarctic ice shelves (the floating extensions of ice sheets [1], [2]) and the corresponding decrease in the restraint experienced by inland ice flow [3], [4] are recognized as major drivers of current Antarctic ice loss [5]. Ice shelves play a crucial role in regulating the Antarctic ice discharge into the ocean because they restrain ice flow as they are often laterally constrained by embayments or locally regrounded on rigid obstacles in the bathymetry [6]. Ice-shelf thinning causes an instantaneous acceleration and a retreat of the grounding line, i.e., the limit between the grounded ice sheet and the floating ice shelf [7]. These consequences lead to an increase in ice discharge into the ocean, hence a contribution to sea level rise.

Radar remote sensing, and interferometry, in particular, is an essential tool to monitor ice-shelf behavior by deriving ice flow fields and tracking grounding line positions over time, among others. This has led to the continental-wide mapping of the surface velocities in Antarctica [8], which is the basis for all major ice-sheet model predictions [9]. Ice velocity is also essential for determining the current state of the ice sheet to determine its basinwise mass balance through the input–output method, in combination with atmospheric modeling [5].

Using pairs of synthetic aperture radar (SAR) images, it is possible to derive surface velocity of the Antarctic ice shelves. Depending on the speed of the ice flow, the SAR sensor and the revisit time of the satellite, one can use techniques based on local correlation maximization, namely speckle tracking [10]–[12] or based on phase shifts measurement using differential SAR Interferometry (DInSAR)[13]. The latter is one order of magnitude more precise, but often less widely applicable. Over ice shelves, the location of individual scatterers can rapidly move from one acquisition to another, leading to important coherence losses if their relative displacement between two dates is greater than a fraction of the wavelength. Adding snow accumulation and compaction, these temporal decorrelation sources are the main limiting factors in SAR interferometry when studying ice sheet [14], [15]. Nevertheless, the subcentimeter accuracy of

Manuscript received February 24, 2020; revised May 3, 2020 and June 30, 2020; accepted July 7, 2020. Date of publication July 10, 2020; date of current version July 24, 2020. This work was supported by the French Community of Belgium in the funding context of an FRIA grant and carried out in the framework of the MIMO (Monitoring melt where Ice Meets Ocean) Project funded by the Belgian Science Policy contract SR/00/336. *(Corresponding author: Quentin Glaude.)*

Quentin Glaude is with the Laboratoire de Glaciologie, Université libre de Bruxelles, 1050 Brussels, Belgium, and also with the Centre Spatial de Liège, Université de Liège, 4031 Angleur, Belgium (e-mail: qglaude@ulb.ac.be).

Charles Amory is with the Laboratoire de Climatologie, Université de Liège, 4031 Liège, Belgium (e-mail: charles.amory@uliege.be).

Sophie Berger is with the Alfred-Wegener-Institut Helmholtz-Zentrum für Polar-und Meeresforschung, 27570 Bremerhaven, Germany (e-mail: sophie.berger@awi.de).

Dominique Derauw is with the Centre Spatial de Liège, Université de Liège, 4031 Angleur, Belgium, and also with the Instituto de Investigación en Paleobiología y Geología, Universidad Nacional De Rio Negro, 27570 General Roca, Argentina (e-mail: dderauw@uliege.be).

Frank Pattyn is with the Laboratoire de Glaciologie, Université libre de Bruxelles, 8332 Brussels, Belgium (e-mail: fpattyn@ulb.ac.be).

Christian Barbier and Anne Orban are with the Centre Spatial de Liège, Université de Liège, 4031 Angleur, Belgium (e-mail: cbarbier@ulg.ac.be; aorban@ulg.ac.be).

Digital Object Identifier 10.1109/JSTARS.2020.3008497

differential SAR interferometry makes it a first-choice technique for ice motion estimation [16], provided that the method is applicable. For example, Mouginot *et al.* [17] achieved 20 cm·a^{-1} velocity accuracy in the interior part of the Antarctic ice sheet, using multiple SAR satellites from ERS to ALOS PALSAR 2.

Unfortunately, for ice shelves, an additional problem appears. When entering the ocean, the ice sheet slowly begins to float and is subject to sea-level fluctuations. These fluctuations will impact the displacement measurement in differential SAR interferometry and, consequently, the horizontal velocity. These vertical displacements are due, on the one hand, to the effects of tides and, on the other hand, to variations in the atmospheric pressure between two dates, causing a hydrostatic readjustment, known as inverse barometer effect (IBE) [18]. Moreover, when studying an area over a short time interval, errors in the velocity estimation are even more accentuated. Working with Sentinel-1 SAR acquisitions at a 6-day revisit time, the vertical bias can be as important as the horizontal velocity that has to be measured.

Compared to previous satellite systems, Sentinel-1's high repeat pass cycle (6–12 days) now allows the evaluation of changes on short time scales, whereas previously, only a mean state could be determined. This has already allowed the determination of subshelf melt rates over periods of 1–2 years using Lagrangian techniques [19]–[21]. However, determining the basal mass balance of the ice shelves requires precise velocity divergence fields, which still contain large errors to be accounted for. This paradigm shift in earth observation enables us to study subtle changes in ice dynamics. Nevertheless, these changes are within the error interval produced by tides and IBE, among others, thus require the development of correction methods.

Tides and IBE biases are well-known problems in DInSAR applied in glaciology. Some authors have confronted the physics of the problem, trying to model the ice-shelf bending, according to ice rheology [22]–[26]. While being very efficient, these ice flexure models are also complicated to adapt in every real case study. For instance, the topography of the study area (pinning points, bathymetry, embayment, etc.) brings a complexity rarely taken into account in these models. Other researchers have also developed empirical methods [27]–[30] to correct for tide-related vertical motions, for example by temporally aggregating ERS-1/2 results over longer time series [27], or by computing the deflection ratio to correct tides/IBE biases on Cosmo-Skymed results [28], [29].

In this article, we describe a fast implementable empirical technique that is capable of removing the main contribution of vertical displacements using double difference SAR interferograms and geophysical models. Using some hypotheses, it also avoids the use of more complex ice physics solutions. The method is presented in Section II. In Section III, we present the study case, the Sentinel-1 SAR images, and the geophysical models used in the study. Section IV exposes the results obtained over the Roi Baudouin Ice Shelf (RBIS), located in Dronning Maud Land, East Antarctica. Section V provides concluding remarks. Finally, uncertainty propagation of the method is formalized in Appendix.

II. Methodology

A. Differential SAR Interferometry

Interferometry is the superposition of two coherent wavefronts, resulting in a fringe pattern that depends on the local optical path differences. In SAR interferometry (InSAR), this fringe pattern is produced by multiplying the first SAR image by the complex conjugate of the second SAR image leading directly to the interferometric phase. This InSAR phase being the subtraction of the phase of each of the two SAR images, it is directly proportional to the local optical path difference [13].

In terms of phase, this optical path difference is made up by five different terms, namely the orbital phase ϕ_{orb}, the topographic phase ϕ_{topo}, the displacement phase $\phi_{\mathrm{displ_{LOS}}}$, in the line-of-sight (LOS) direction, the atmospheric phase screen ϕ_{atm}, and an additional noise ϕ_{noise}, given by

$$\begin{aligned}\phi_{\mathrm{InSAR}} &= \phi_{\mathrm{t_2}} - \phi_{\mathrm{t_1}} \\ &= \phi_{\mathrm{orb}} + \phi_{\mathrm{topo}} + \phi_{\mathrm{displ_{LOS}}} + \phi_{\mathrm{atm}} + \phi_{\mathrm{noise}}. \end{aligned} \quad (1)$$

Differential SAR Interferometry allows the measure of the phase component related to displacements. Knowing the orbits of the satellites and the topography of the region, the first two terms can be estimated and removed from (1). Precise orbits are generated by the Copernicus Precise Orbit Determination Service. For topography, we use the Dronning Maud Land TanDEM-X DEM created by the Alfred-Wegener Institute [31]. If the atmospheric and noise phase components can be neglected or corrected [32], the differential phase obtained after removing the geometric component is retrieved, leading to direct estimation of the LOS displacement component. The relation between the differential interferometric phase and the LOS displacement is given by

$$\phi_{\mathrm{displ_{LOS}}} = \frac{4\pi}{\lambda} \cdot \mathrm{displ_{LOS}} \quad (2)$$

where λ is the radar wavelength (0.0556 m in the case of Sentinel-1) and $\mathrm{displ_{LOS}}$ is the estimated displacement in meters. Considering the time lapse between SAR acquisitions in the DInSAR processing, we finally obtain the velocity.

Since SAR sensors are side looking, they measure the vector sum of both the vertical and horizontal displacements ($\mathrm{displ_H}$ and $\mathrm{displ_V}$), projected along the LOS according to the incidence angle θ, given by

$$\mathrm{displ_{LOS}} = \mathrm{displ_H} \cdot \sin\theta + \mathrm{displ_V} \cdot \cos\theta. \quad (3)$$

The last component of the 3-D deformation vector, the along-track displacement, cannot be reliably estimated from a single SAR interferogram.

Separating both the vertical and the horizontal components can only be performed using different viewing geometries or using *a priori* knowledge of the observed displacements (e.g., assuming the determined ice flow only follows the surface slope). From (3), we understand that interpreting the LOS measurement as it comes from a purely horizontal displacement while a vertical one is also present will induce a bias.

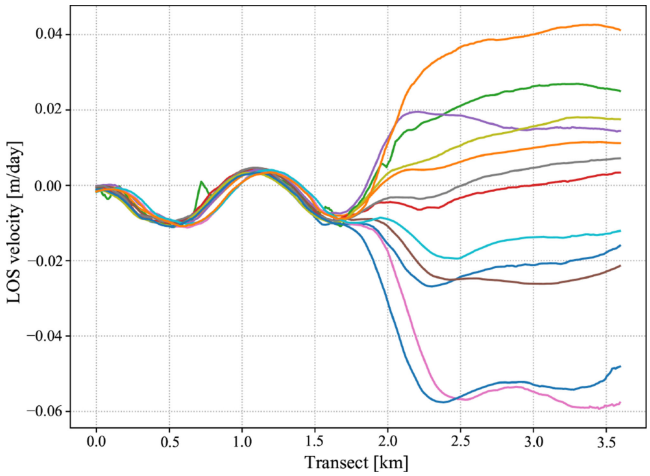

Fig. 1. Sentinel-1 DInSAR-based LOS velocity changes through a transect crossing the grounding zone (70° 45′S, 24°40′E), over the period December 2018 to August 2019. Each curve represents a velocity profile determined from 6-day displacements. The velocity change has been set to zero at the start of the transect. Without correction, a vertical displacement brings an additional phase pattern over the ice shelf, which changes significantly for every pair of dates. This effect is negligible over the grounded ice in our region.

B. Tides and IBE

Horizontal and vertical components of the displacement are related to different geophysical processes, which cannot be measured separately without prior hypothesis. Over ice shelves, the horizontal displacements are caused by a horizontal motion of ice that can reach several hundreds of meters per year. These ice shelves move by spreading, due to the pressure balance of the ocean water against the ice front. This horizontal displacement is assumed stable from one acquisition to the other, on a sub-monthly basis [28], [29], though small tidally induced variations can be observed [33]. On the other hand, the vertical displacements of ice shelves are mainly due to short-term variations of the local sea level, which are influenced by tides and variable atmospheric pressure [18].

On the grounded part of the ice sheet, the displacement response to the tides and pressure variations is negligible. On the floating part, which is in hydrostatic equilibrium, the vertical displacement of the ice strictly follows the oceanic readjustment (tides/IBE). In the grounding zone—the transition area between grounded and floating areas—the progressive response to oceanic readjustment is translated into a high fringe rate in the differential interferogram. Converted into velocity, the vertical displacement strongly affects the measure of the surface velocity (see Fig. 1).

Considering a 6-day revisit time (Sentinel-1 in EW mode) and an incidence angle of 33°, erroneously interpreting a 1-m vertical displacement induces a bias of ± 95 m·a^{-1} in the resulting horizontal flow field. In low-velocity areas, this bias is of the same order of magnitude as the measured speed, misleading the interpretation of the ice dynamics. While increasing the temporal baseline between SAR images may reduce the relative influence of the vertical displacements, it also critically increases the temporal decorrelation and leads to an incoherent interferometric signal.

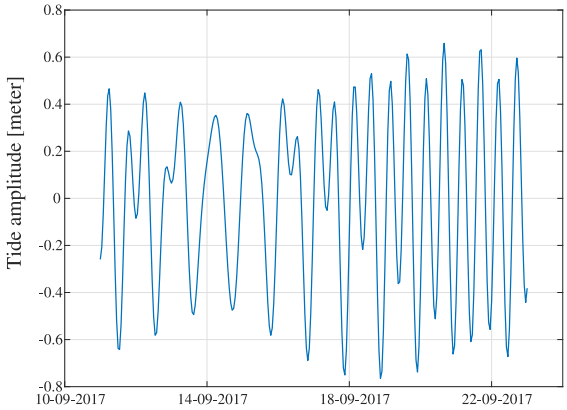

Fig. 2. Tide amplitude estimation between 12 days using CATS2008 model [35] over the RBIS (70°54′S, 26° 24′E). Vertical displacements are rapidly varying, even on short timescales.

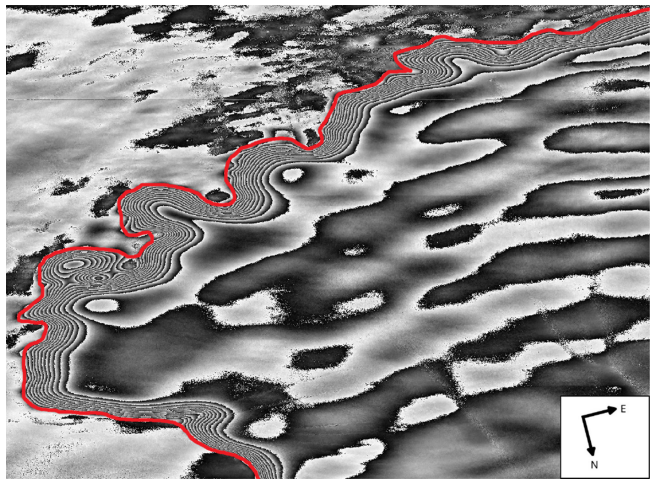

Fig. 3. Double difference Interferogram, represented in azimuth-range geometry. This particular interferogram contains mainly vertical displacement phase components. On the figure, we can delineate the floating from the grounded ice areas thanks to the high fringe pattern, representing the grounding zone. The grounding line is represented in red.

C. Empirical Removal of the Vertical Bias

Over short periods, we can assume that between successive SAR pairs, ice-shelf velocity is constant [29], and observed changes are attributed to rapid fluctuations of tides and IBE. This can be observed estimating tidal amplitudes using the CATS2008 tide model [34], [35] over the RBIS on short time period (see Fig. 2).

Subtracting two consecutive differential interferograms yields a double difference interferogram (double DInSAR or DDInSAR, Fig. 3). This DDInSAR contains the changes in the ice-shelf velocity. These changes are mainly vertical (following the sea-level adjustment to tides and IBE) but small tidally induced horizontal variations can also be observed [25]

$$\begin{aligned}\phi_{\mathrm{DDInSAR}} &= \phi_{\mathrm{DInSAR}_2} - \phi_{\mathrm{DInSAR}_1} \\ &\approx \cancel{\phi_{\mathrm{displ}_{\mathrm{H}_2}}} + \phi_{\mathrm{displ}_{\mathrm{V}_2}} - \left(\cancel{\phi_{\mathrm{displ}_{\mathrm{H}_1}}} + \phi_{\mathrm{displ}_{\mathrm{V}_1}}\right) \\ &\approx \phi_{\mathrm{displ}_{\mathrm{V}_2}} - \phi_{\mathrm{displ}_{\mathrm{V}_1}}. \end{aligned} \quad (4)$$

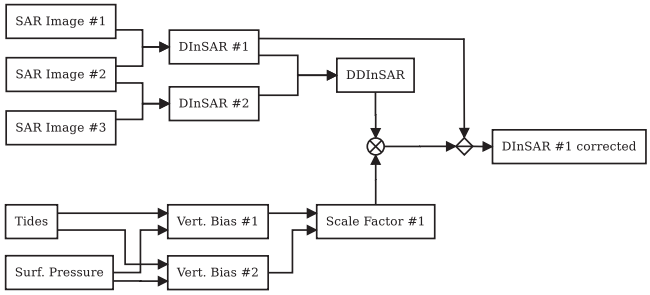

Fig. 4. Flowchart of tides/IBE correction. From three SAR acquisitions, two consecutive differential interferograms can be created. Using geophysical models, vertical biases of each DInSAR is computed (5) at any given position. Finally, a DDInSAR is created (4). This DDInSAR is rescaled to match the vertical bias of the DInSAR, then removed (6). The same reasoning is applied to correct the second differential interferogram. The unwrapping process is not represented here.

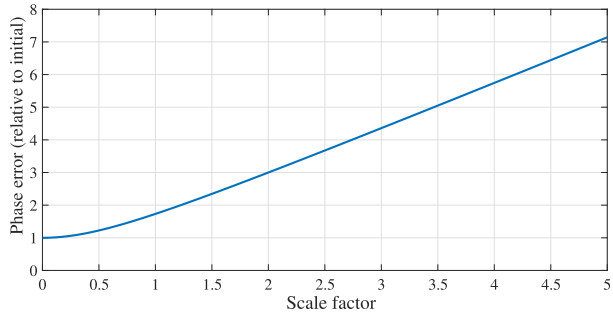

Fig. 5. Standard deviation of the corrected interferogram as a function of the DDInSAR scale factor $\frac{\Delta z_1}{\Delta z_2 - \Delta z_1}$. The more similar the vertical biases, the greater the scale factor and *in fine* the less accurate the correction. Displacement accuracy is linearly dependent on the interferometric phase error.

$\phi_{\mathrm{displ}_{\mathrm{H}_1}}$ is associated with horizontal displacements of the ice shelf between the first two SAR acquisition dates, whereas $\phi_{\mathrm{displ}_{\mathrm{V}_1}}$ corresponds to ice-shelf displacements related to a vertical change Δz_1 of the sea level. Similarly, $\phi_{\mathrm{displ}_{\mathrm{H}_2}}$ and $\phi_{\mathrm{displ}_{\mathrm{V}_2}}$ are related to the displacements between the two following SAR acquisitions dates. The oceanic vertical displacement Δz at a given location (x, y) and time period t is defined by

$$\Delta z_t(x,y) = \Delta\mathrm{tides}_t(x,y) - \Delta\mathrm{pressure}_t(x,y). \tag{5}$$

A difference of tidal amplitudes directly gives the vertical displacement: a positive Δtides is translated into a positive vertical bias, meaning an upward displacement. On the contrary, varying pressure differences Δpressure need to be converted into metric oceanic readjustment. The theoretical IBE value is -1 cm·hPa^{-1} [34], although this theoretical value can slightly change over the different ice shelves or coastal areas [18].

From (4), ϕ_{DDInSAR} (see Fig. 3) is associated with the vertical displacement $\Delta z_2 - \Delta z_1$ between the two considered interferometric pairs. From this double difference fringe pattern, it is possible to distinguish the grounded area (not affected by tides) from the floating area (in hydrostatic equilibrium), with a high-fringe transition corresponding to the grounding zone. This property was already used in [31] and [36] to define the position of the grounding line.

To remove the vertical bias of each differential interferogram, we need to subtract the corresponding vertical phase component. This vertical bias can be estimated by properly rescaling the unwrapped DDInSAR phase component

$$\begin{aligned}\phi_{\mathrm{displ}_{\mathrm{H}_1}} &= \phi_{\mathrm{DInSAR}_1} - \phi_{\mathrm{displ}_{\mathrm{tide/IBE}_1}} \\ &= \phi_{\mathrm{DInSAR}_1} - \tfrac{\Delta z_1}{\Delta z_2 - \Delta z_1} \cdot \phi_{\mathrm{DDInSAR}}\end{aligned} \tag{6}$$

where $\frac{\Delta z_1}{\Delta z_2 - \Delta z_1}$ is the scale factor applied to the DDInSAR to correct for the bias caused by Δz_1 present in the first differential interferogram DInSAR_1. Fig. 4 represents a simplified flowchart of the tides/IBE correction. One important aspect of this technique is that the DDInSAR simulates the flexure of the ice by assuming elastic behavior, putting aside concepts of ice rheology, such as ice viscosity, flexural rigidity, Young's modulus, or Poisson's ratio. While viscoelastic modeling better represents the bending process in some circumstances, especially at low tide [25], the residuals remain small compared to the tides/IBE bias.

D. Variance Propagation

The scale factor $\frac{\Delta z_1}{\Delta z_2 - \Delta z_1}$ has an important consequence in the estimated accuracy of the corrected interferogram. Focusing only on the interferometric noise, variance propagation of the correction (6) can be expressed as

$$\sigma^2_{\mathrm{corrected}} = \begin{pmatrix} 1 & \frac{\Delta z_1}{\Delta z_2 - \Delta z_1} \end{pmatrix} \cdot \begin{pmatrix} \sigma_{\mathrm{D}} & 0 \\ 0 & \sigma_{\mathrm{DD}} \end{pmatrix} \cdot \begin{pmatrix} 1 \\ \frac{\Delta z_1}{\Delta z_2 - \Delta z_1} \end{pmatrix} \tag{7}$$

where σ_{D} and σ_{DD} are the phase standard deviations of the differential interferogram and the double difference interferogram, respectively. For a pair of interferograms with similar phase standard deviation, this expression leads to

$$\sigma_{\mathrm{corrected}} = \sigma_{\mathrm{D}} \cdot \sqrt{1 + 2 \cdot \left(\tfrac{\Delta z_1}{\Delta z_2 - \Delta z_1}\right)^2}. \tag{8}$$

This expression is represented in Fig. 5. Since the displacement accuracy is directly proportional to $\sigma_{\mathrm{corrected}}$, it demonstrates the importance of the scale factor in the processing. In cases where interferograms involved in the correction have similar vertical biases, we are more likely to increase the scale factor and consequently the phase noise after correction. Formal quantification of uncertainty is available in the Appendix, including the influence of tidal and atmospheric pressure accuracy, with numerical examples. Depending on the image geometry, coherence, and scale factor, the precision of the corrected horizontal velocity ranges from less than a meter per year accuracy to a few meters per year. If above, we need to consider correcting or not, depending on the interferogram.

E. Network of DInSARs

With a minimum of three SAR images, we can correct the vertical bias related to tides and IBE. However, if we have more data available, we can overconstrain the problem. Each SAR image is combined to its closest acquisition in time to make a

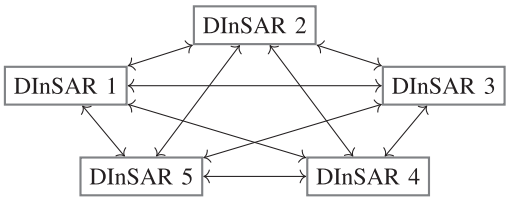

Fig. 6. Interaction graph between five interferograms. In this configuration, each differential interferogram can be corrected four times. Overconstrained problems allow the user to select the DDInSAR that minimizes the scale factor.

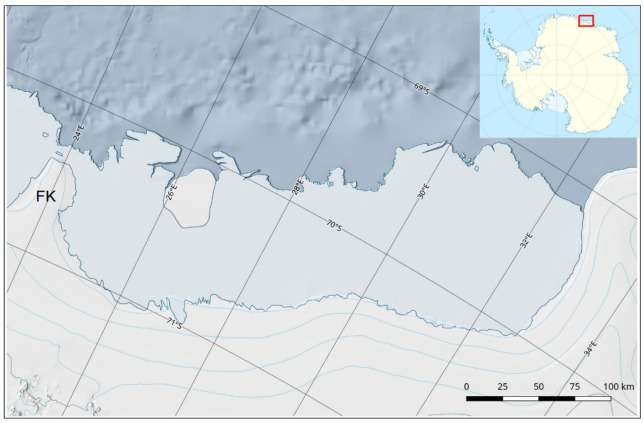

Fig. 7. RBIS, Dronning Maud land, Antarctica. FK: Fran-Kenny Ice Rise. Basemap from [40], with modifications.

differential interferogram. These DInSARs are then connected, generating several double difference interferograms. These connections open up new possibilities for correcting each interferogram, adding several degrees of freedom in our problem. In a configuration where five DInSAR are available, for instance, each differential interferogram can be corrected four times (see Fig. 6). Each of the possible correction introduces a unique scale factor. Having the possibility to select how the interferogram is corrected allows us to select the DInSAR pairs that minimize the scale factor in (6) and (8), reducing the estimated phase variance of the corrected interferogram, and so the uncertainty of the ice-flow fields.

III. Data

A. Study Case

Our test case focuses on the RBIS, -24 to $-33°$ East), Dronning Maud Land, East Antarctica (see Fig. 7). RBIS has presumably been stable for several millennia [37], [38]. The ice shelf is fed by the Ragnhild glaciers. On the western part of the RBIS, velocity reaches 0.82 m per day (300 m·a^{-1}), and have not changed significantly since the 1960s [39]. It is far from spatially homogeneous, and velocity can go below than 100 m·a^{-1}.

B. SAR Data

In the frame of this work, we used Sentinel-1 SAR single-look-complex (SLC) acquisitions in interferometric wide (IW) swath and extra wide (EW) swath modes. For each mode, we selected image pairs keeping a high interferometric coherence. IW and EW distinguish themselves by their spatial resolution and coverage. The resolution of IW allows SLC images with a pixel spacing of 2.3 × 14.1 m (range × azimuth). The three subswaths obtained by this acquisition mode covers a width of about 250 km. In EW, the swath coverage is increased to 400 km at the cost of a coarser resolution (and increased pixel spacing, i.e., 5.9 × 19.9 m).

TABLE I
S1 IW SLC TOPS Acquisitions

SAR Acquisition Date	Time (utc)	Relative Orbit	Pixel Spacing (m)
11/09/2017	18h45	59	2.3x14.1
23/09/2017	18h45	59	2.3x14.1
05/10/2017	18h45	59	2.3x14.1
17/10/2017	18h45	59	2.3x14.1

TABLE II
S1 EW SLC TOPS Acquisitions

SAR Acquisition Date	Time (utc)	Relative Orbit	Pixel Spacing (m)
Period 1			
01/12/2018	18h30	88	5.9x19.9
07/12/2018	18h30	88	5.9x19.9
13/12/2018	18h30	88	5.9x19.9
19/12/2018	18h30	88	5.9x19.9
25/12/2018	18h30	88	5.9x19.9
31/12/2018	18h30	88	5.9x19.9
Period 2			
11/02/2019	18h30	88	5.9x19.9
17/02/2019	18h30	88	5.9x19.9
23/02/2019	18h30	88	5.9x19.9
01/03/2019	18h30	88	5.9x19.9
Period 3			
18/04/2019	18h30	88	5.9x19.9
24/04/2019	18h30	88	5.9x19.9
30/04/2019	18h30	88	5.9x19.9
06/05/2019	18h30	88	5.9x19.9

In IW mode, the revisit time over the RBIS is 12 days. We selected a set of four acquisitions for the experiment (see Table I).

For the EW mode, we employed acquisitions from December 2018 to August 2019, with a 6-day revisit time. From this time series, we computed each possible 6-day full-resolution interferogram. We discarded interferogram with coherence below 0.6 over the ice shelf. Finally, we selected the following three periods with useful interferograms (see Table II).

1) *December 2018*: Five successive differential interferograms on a one-month time period.
2) *February 2019*: Two differential interferograms from four consecutive SAR pairs.
3) *April 2019*: Three successive differential interferograms from four consecutive SAR pairs.

The December 2018 time period is particularly interesting because of the number of potential interconnections, as detailed in Section II-E. With five consecutive interferograms, each DInSAR has four possible corrections.

C. Tides and Regional Climate Models

The computation of tides is performed using the CATS2008 model [35]. CATS2008 is a regional high-resolution ocean tide and ocean tide loading model that uses, among others, the ten major tidal components. Besides, the model can produce tide estimates over ice-shelf areas. Linear regression analysis between

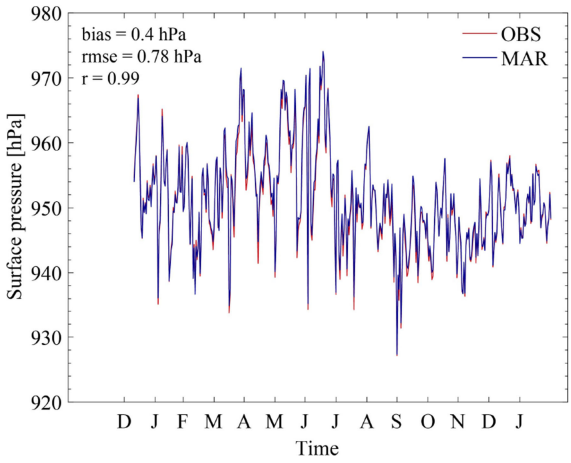

Fig. 8. Comparison of daily mean surface pressure simulated by MAR (blue) and measured on the Fran-Kenny ice rise (red) (see Fig. 7) for the period December 2017–January 2019.

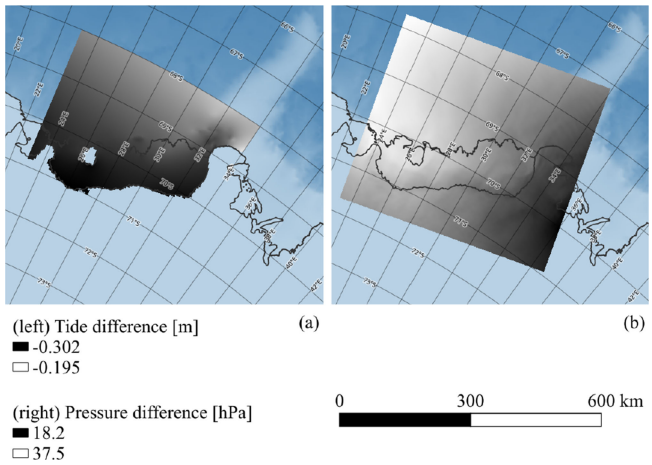

Fig. 9. (a) Modeled tides difference obtained from CATS2008 and (b) modeled surface pressure difference obtained from MAR simulations between October 17th, 2017 and October 5th, 2017. Spatial variability on large scale requires the computation of the vertical bias on grid covering the study area.

InSAR-based vertical displacements and the CATS2008 model predictions, corrected from IBE, shows a coefficient of determination of 0.938 and a root-mean-square error of 0.5 cm [28]. Over the RBIS, the tidal amplitudes from CATS2008 vary within less than 2 m.

Surface pressure fields are obtained from the regional climate model MAR version 3.10, which is among the state-of-the-art regional climate models to simulate near-surface climate and surface mass balance of the Antarctic ice sheet [16]. MAR has been run at a high spatial resolution (5-km horizontal gridding) on a domain focusing on the RBIS, and forced at its lateral boundaries by atmospheric profiles (pressure, wind speed, temperature, and specific humidity) and at the ocean surface by sea-surface temperatures and sea-ice concentration from ERA5 reanalysis fields [41]. The forcing is prescribed every 6 h, and the model can evolve freely in its inner spatial domain. Simulated surface pressure compares well ($r > 0.99$) with observed surface pressure on the Fran-Kenny Ice Rise (70.3° S, 24.18° E, 266-m asl) west of the RBIS (see Fig. 7), over the period December 2017 to January 2019 (see Fig. 8).

Both tides and atmospheric pressure are slowly varying in space. That allowed some studies to compute tidal estimates at a single location, considered spatially constant over the entire studied region. While this remains true for satellites with low spatial coverage, keeping this hypothesis valid becomes more challenging over wide areas, such as Sentinel-1 250- or 400-k swath coverage, depending on the acquisition mode. Therefore, the vertical bias should be computed on an interpolated grid covering the study area. For instance, components of the vertical bias computed for the October 5th and 17th, 2017 SAR pair are represented in Fig. 9.

IV. Results

Our results show that the correction brings a totally different interpretation of the fringe pattern (see Figs. 10 and 12). For the IW case (see Fig. 10), if interpreting the fringe pattern as

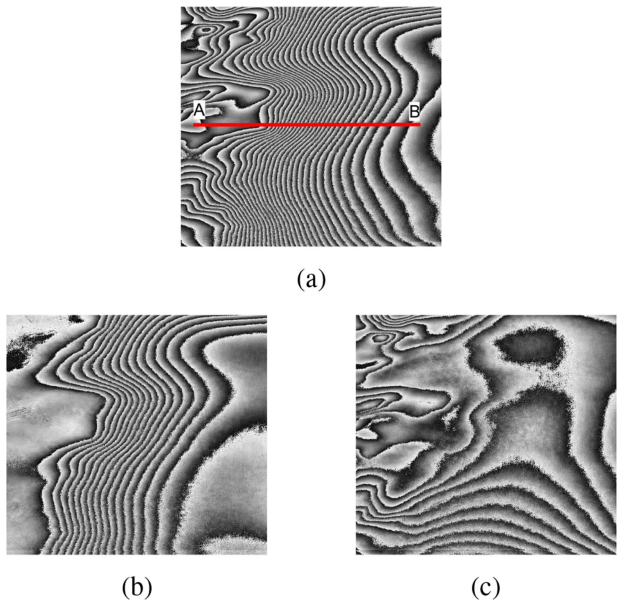

Fig. 10. Correction of a DInSAR over the grounding zone, IW case (70°45′S, 24°40′E, with acquisition geometry presented in Fig. 3). (a) Noncorrected DInSAR, (b) rescaled rewrapped DDInSAR, corresponding the vertical phase bias, and (c) corrected DInSAR. Vertical biases phase component is captured through the DDInSAR, which is rescaled then removed from the interferogram. A 4-km profile is visible in Fig. 11.

only due to horizontal displacements, one would observe an unrealistic sudden horizontal acceleration along the profile in Fig. 10(a). This fringe rate is an artifact resulting from vertical displacement, as already observed in Fig. 1. The proposed technique used here allows the estimation and removal of the corresponding bias [see Fig. 10(b) and (c)].

The profile across Fig. 10(a) shows the difference between the LOS displacement with and without correction (see Fig. 11). The estimated LOS velocity without correction shows a 24 m·a^{-1} velocity at the edge of the transect. Interpreting it as solely due

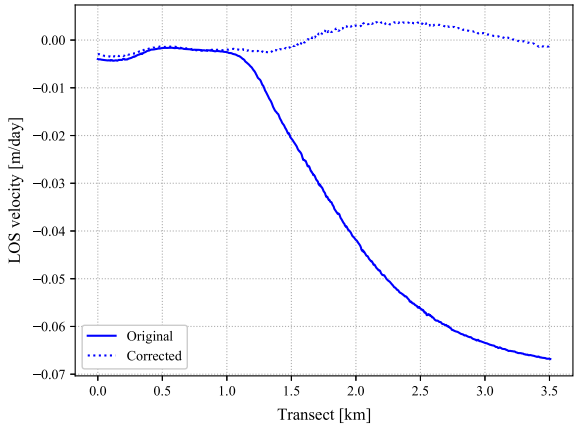

Fig. 11. Comparison between the LOS velocity through a 4-km profile, visible in Fig. 10. The correction manages to reduce the important velocity deviation that occurred in the grounding zone.

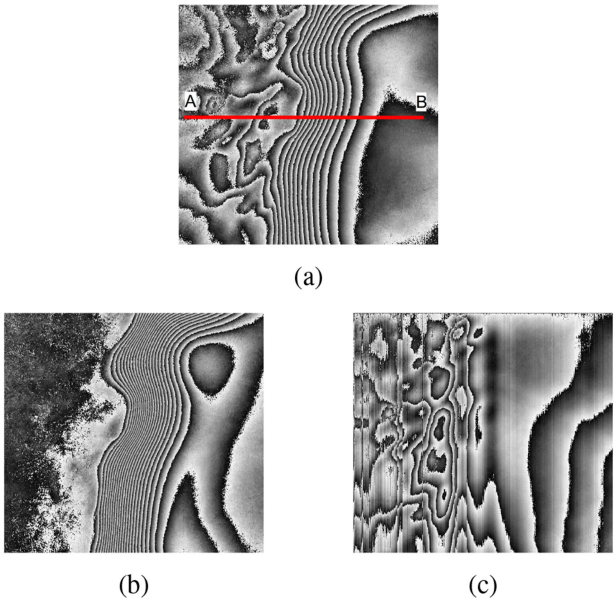

Fig. 12. Correction of a DInSAR over the grounding zone, EW case (70°45′S, 24°40′E, with acquisition geometry presented in Fig. 3). (a) Non-corrected DInSAR, (b) DDInSAR, and (c) corrected DInSAR. A 4-km profile is visible in Fig. 13.

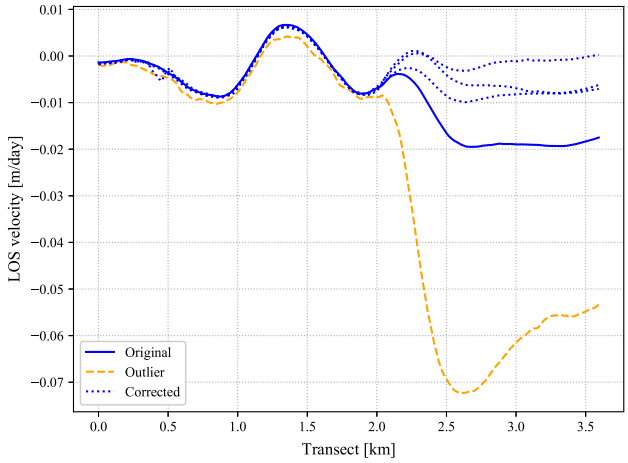

Fig. 13. LOS velocity profiles through a transect crossing the grounding zone (see Fig. 12). The solid blue line represents the LOS velocity prior correction. Over the four possible corrections (dotted curves), three results produced similar corrections (dotted blue). The orange dotted curve represents the correction in a nondeal case, with a scale factor greater than 10.

TABLE III
TIDES AND PRESSURE ESTIMATION FOR DECEMBER 2018 PERIOD (70°54′S, 26°24′E)

SAR Acquisition Date	Time (utc)	pressure [hPa]	tide [m]
01/12/2018	18h30	985.951	-0.2548
07/12/2018	18h30	971.125	0.4156
13/12/2018	18h30	970.732	0.1626
19/12/2018	18h30	983.402	0.0575
25/12/2018	18h30	982.877	0.4597
31/12/2018	18h30	973.336	0.0056

TABLE IV
NUMERICAL EXAMPLE OF DECEMBER 2018 PERIOD CORRECTION—SENTINEL-1 EW MODE (70°54′S, 26°24′E)

DDInSAR	Δz_1 [m]	Δz_2 [m]	Scaling 1	Scaling 2
(2)-(1)	0.818	-0.249	-0.767	0.233
(3)-(2)	-0.231	-0.249	**13.473**	**14.473**
(4)-(3)	0.407	-0.231	-0.637	0.363
(5)-(4)	-0.358	0.407	-0.468	0.532
(5)-(1)	-0.358	0.818	-0.305	0.695
(3)-(1)	-0.231	0.818	-0.221	0.779
(4)-(1)	0.407	0.818	0.991	1.991
(4)-(2)	0.407	-0.249	-0.621	0.379
(5)-(2)	-0.358	-0.249	-3.269	-2.269
(5)-(3)	-0.358	-0.231	-2.826	-1.826

to horizontal displacements and with an incidence angle of 21°, this value translates as 67 m·a^{-1}. After correction, we observe a more realistic displacement of the ice flow, although we also observe a small overshoot, suggesting a slight overcorrection. Nevertheless, the fringe cleaning observed in Fig. 10 shows the validity of the proposed approach. Indirectly, it also constitutes a cross validation of the used tidal and IBE models. Similar observations are met for the EW Sentinel-1 mode (see Figs. 12 and 13). Using consecutive interferograms, we can overconstrained the problem. In Fig. 13, all the different possible solutions are between a few meters per year velocity.

As suggested by (8) and in the Appendix, the technique may amplify the noise component of the interferogram. The effect can be highly pronounced in the case of an important scale factor $\frac{\Delta z_1}{\Delta z_2 - \Delta z_1}$ in (6), when Δz_1 is, by chance, close to Δz_2.

This case arose with some of the EW SAR images. Focusing on December 2018 period, we compute for each SAR image the atmospheric pressure (MAR) and the tides (CATS2008). Numerical values for one given position on the RBIS are displayed in Table III, as an example. Based on these values, we can, for each successive interferogram, compute the vertical bias given by (6). As such we can form the double difference interferograms and compute the scale factors to be applied to the DDInSAR to correct each interferogram (see Table IV). In the second row, in bold, the vertical bias of the second and the third interferograms are very similar, resulting in an important scale factor (13.473).

In these cases, the correction is unlikely to produce satisfying results, as shown by the orange curve in Fig. 13.

V. Conclusion

Ice shelves are subject to vertical fluctuations related to tides and varying atmospheric pressure, which introduce a bias in the computation of the horizontal displacements by differential SAR interferometry. This effect propagates in the velocity estimation, whose errors are further amplified by the short revisit time of current SAR satellites, such as Sentinel-1. For instance, this bias can reach up to 0.25 m·day^{-1} absolute horizontal velocity anomaly with 6-day interferograms, if not corrected. In these cases, this artifact can be as important as the horizontal velocity. Recent SAR satellites have shorter revisit time, which allows the study of ice dynamics and ice shelves at near-continuous timescales. These improvements go along with technical adaptations, which in this case consists of correcting the velocity fields.

Here, we propose a simple approach to correct differential interferograms using scaled double difference interferograms to estimate the phase component due to vertical displacements; this scaling factor being computed from CATS2008 tides and a regional climate model (MAR). The method represents the ice flexure by assuming elastic behavior. It brings a rapid solution to a complex problem while still managing to remove the major contribution due to vertical biases. Working at short timescales over large areas makes the technique in line with current and future SAR satellite constellations.

Results on RBIS with Sentinel-1 in IW and EW modes demonstrate the applicability of the technique. Nevertheless, the technique can suffer from CATS2008/MAR model uncertainties, especially when these estimates are similar from different dates (see Section II-D and Appendix). If the acquisition plan allows us to use more than two SAR pairs, we can overconstrain the problem and limit this effect by selecting the differential interferograms that minimize the estimated phase standard deviation.

The method is sensor independent. In particular, it would be useful to apply it to other sensors, specifically when the revisit time is low, such as Cosmo-Skymed or Radarsat Constellation Mission for example (1 and 4 days, respectively).

Appendix
Uncertainty Propagation of the Method

In this article, a tides/IBE correction has been proposed (6)

$$\phi_{\mathrm{displ}_{\mathrm{H}_1}} = \phi_{\mathrm{DInSAR}_1} - \frac{\Delta z_1}{\Delta z_2 - \Delta z_1} \cdot \phi_{\mathrm{DDInSAR}}. \quad \text{(A.9)}$$

Tides and atmospheric pressure modeling are tainted with errors, as well as the interferometric phase. These errors are gradually propagated through the method.

The variables that intervene are as follows:

1) the tide, estimated with a precision σ_{tide};
2) the atmospheric pressure, estimated with a precision σ_{pres};
3) the phase of the differential interferogram, estimated with a precision σ_{D}; and
4) the phase of the double difference interferogram, estimated with a precision σ_{DD}.

The tides and atmospheric pressure are computed independently for each acquisition date. Then, between two dates, a difference of tides and atmospheric pressure is estimated. The resulting difference of tides $\Delta\mathrm{tides}$ is estimated with a precision $\sqrt{2} \cdot \sigma_{\mathrm{tide}}$. Similarly, the difference of atmospheric pressures $\Delta\mathrm{pressure}$ is estimated with a precision $\sqrt{2} \cdot \sigma_{\mathrm{pres}}$. By propagation, the vertical displacement Δz (5) is estimated with a precision $\sqrt{2} \cdot \sqrt{\sigma^2_{\mathrm{tide}} + \sigma^2_{\mathrm{pres}}}$.

This leads us to the scale factor $\frac{\Delta z_1}{\Delta z_2 - \Delta z_1}$. Each Δz_i is considered independent and attached with the precision $\sqrt{2} \cdot \sqrt{\sigma^2_{\mathrm{tide}} + \sigma^2_{\mathrm{pres}}}$. The variance of the scale factor $\sigma^2_{\mathrm{scale}}$ is given by the nonlinear propagation of uncertainty

$$\sigma^2_{\mathrm{scale}} = J \cdot \Sigma \cdot J^T \quad \text{(A.10)}$$

with

$$\Sigma = \begin{pmatrix} 2 \cdot (\sigma^2_{\mathrm{tide}} + \sigma^2_{\mathrm{pres}}) & 0 \\ 0 & 2 \cdot (\sigma^2_{\mathrm{tide}} + \sigma^2_{\mathrm{pres}}) \end{pmatrix} \quad \text{(A.11)}$$

and

$$\begin{aligned} J &= \begin{pmatrix} \frac{\partial \mathrm{scale}}{\partial \Delta z_1} & \frac{\partial \mathrm{scale}}{\partial \Delta z_2} \end{pmatrix} \\ &= \begin{pmatrix} \frac{\Delta z_2}{(\Delta z_2 - \Delta z_1)^2} & -\frac{\Delta z_1}{(\Delta z_2 - \Delta z_1)^2} \end{pmatrix} \end{aligned} \quad \text{(A.12)}$$

which leads to

$$\sigma_{\mathrm{scale}} = \frac{\Delta z_1 + \Delta z_2}{(\Delta z_2 - \Delta z_1)^2} \cdot \sqrt{2} \cdot \sqrt{\sigma^2_{\mathrm{tide}} + \sigma^2_{\mathrm{pres}}}. \quad \text{(A.13)}$$

Finally, the full variance propagation of the correction proposed in (6) can be expressed as [similar reasoning as for (A.13)]

$$\sigma^2_{\mathrm{corrected}} = J \cdot \Sigma \cdot J^T \quad \text{(A.14)}$$

with

$$\Sigma = \begin{pmatrix} \sigma^2_{\mathrm{D}} & 0 & 0 \\ 0 & \sigma^2_{\mathrm{DD}} & 0 \\ 0 & 0 & \sigma^2_{\mathrm{scale}} \end{pmatrix} \quad \text{(A.15)}$$

and

$$J = \begin{pmatrix} 1 & \frac{\Delta z_1}{\Delta z_2 - \Delta z_1} & -\phi_{\mathrm{DD}} \end{pmatrix} \quad \text{(A.16)}$$

For a pair of interferograms with similar phase standard deviation, we can estimate the precision of the double difference to be $\sqrt{2} \cdot \sigma_{\mathrm{D}}$. The resulting standard deviation of the corrected phase is given by

$$\sigma_{\mathrm{corrected}} = \sqrt{\sigma^2_{\mathrm{D}} \cdot (1 + 2 \cdot (\frac{\Delta z_1}{\Delta z_2 - \Delta z_1})^2) + \phi^2_{\mathrm{DD}} \cdot \sigma^2_{\mathrm{scale}}} \quad \text{(A.17)}$$

With $\sigma^2_{\mathrm{scale}}$ expressed in (A.13). σ_{D} can be estimated thanks to the Cramér Rao bound

$$\sigma_{\mathrm{D}} = \frac{1}{\sqrt{2N}} \cdot \sqrt{\frac{1 - \gamma^2}{\gamma^2}} \quad \text{(A.18)}$$

with N the number of looks and γ the interferometric coherence.

Equation (A.17) is the precision associated to the unwrapped corrected interferometric phase. This mathematical expression can be interpreted as follows: first part of the right-hand side expression translates how the scale factor increases the interferometric phase accuracy, whereas the second part expresses how the precision of the scale factor will affect the amount of unwrapped double difference interferometric phase that is removed.

To convert the corrected phase into horizontal velocity error estimates, the factor $\frac{\lambda}{B_t \cdot 4\pi \cdot \sin\theta}$ has to be applied, λ being the wavelength, θ the incidence angle, and B_t the temporal baseline between acquisitions.

As a practical example, with a coherence of 0.8, 12 looks, an incidence angle of 33°, Δz_1 of 0.50 m, Δz_2 of -0.25 m, a tide accuracy of 1 cm, and an atmospheric pressure accuracy of 0.7 hPa, the resulting absolute phase error is 1.104 rad, i.e., 0.55 m·a^{-1} accuracy. If the accuracy of the tides becomes 5 cm, the velocity precision is 2.23 m·a^{-1}, to put in comparison to the -46.8 m·a^{-1} brought by the tides and IBE bias in the first interferogram.

In a less ideal configuration with Δz_2 of 0.40 m, the estimated velocity error of the correction becomes around 7.01 m·a^{-1}.

In Section IV, an extreme case where Δz_1 and Δz_2 are equal to -0.231 and -0.249 m, respectively, is presented. The scale and the uncertainty around this scale factor become too important to use the technique, with an annual velocity precision that can exceed the hundred of meters per year if the tides are poorly estimated.

ACKNOWLEDGMENT

The authors would like to thank J. Lenaerts for providing the weather station data on the Fran-Kenny Ice Rise. They would also like to thank the Norwegian Polar Institute for the Quantarctica package. TanDEM-X data originate from the German Aerospace Center (ATI-GLAC0267).

REFERENCES

[1] H. D. Pritchard, S. R. M. Ligtenberg, H. A. Fricker, D. G. Vaughan, M. R. V. D. Broeke, and L. Padman, "Antarctic ice-sheet loss driven by basal melting of ice shelves," *Nature*, vol. 484, no. 7395, pp. 502–505, 2012. [Online]. Available: http://dx.doi.org/10.1038/nature10968

[2] F. S. Paolo, H. A. Fricker, and L. Padman, "Volume loss from Antarctic ice shelves is accelerating," *Science*, vol. 348, no. 6232, pp. 327–331, 2015. [Online]. Available: https://science.sciencemag.org/content/348/6232/327

[3] A. J. Payne, A. Vieli, A. P. Shepherd, D. J. Wingham, and E. Rignot, "Recent dramatic thinning of largest West-Antarctic ice stream triggered by oceans." *Geophys. Res. Lett.*, vol. 31, 2004, Paper L23401. [Online]. Available: http://dro.dur.ac.uk/1231/

[4] H. D. Pritchard, R. J. Arthern, D. G. Vaughan, and L. A. Edwards, "Greenland and Antarctic ice sheets," *Nature*, vol. 461, no. 7266, pp. 971–975, 2009. [Online]. Available: http://dx.doi.org/10.1038/nature08471

[5] A. Shepherd *et al.*, "Mass balance of the Antarctic ice sheet from 1992 to 2017," *Nature*, vol. 558, no. 7709, pp. 219–222, 2018.

[6] L. Favier and F. Pattyn, "Antarctic ice rise formation, evolution, and stability," *Geophys. Res. Lett.*, vol. 42, no. 11, pp. 4456–4463, 2015. [Online]. Available: https://agupubs.onlinelibrary.wiley.com/doi/abs/10.1002/2015GL064195

[7] D. Goldberg, D. M. Holland, and C. Schoof, "Grounding line movement and ice shelf buttressing in marine ice sheets," *J. Geophys. Res., Earthq. Surf.*, vol. 114, no. F4, 2009, Art. no. F04026. [Online]. Available: https://agupubs.onlinelibrary.wiley.com/doi/abs/10.1029/2008JF001227

[8] E. Rignot, J. Mouginot, and B. Scheuchl, "Ice flow of the Antarctic ice sheet," *Science*, vol. 333, no. 6048, pp. 1427–1430, 2011. [Online]. Available: https://science.sciencemag.org/content/333/6048/1427

[9] L. Favier *et al.*, "Retreat of Pine Island Glacier controlled by marine ice-sheet instability," *Nature Climate Change*, vol. 5, no. 2, pp. 1–5, 2014. [Online]. Available: http://dx.doi.org/10.1038/nclimate2094

[10] L. D. Euillades *et al.*, "Detection of glaciers displacement time-series using SAR," *Remote Sens. Environ.*, vol. 184, pp. 188–198, 2016. [Online]. Available: http://dx.doi.org/10.1016/j.rse.2016.07.003

[11] F. Pattyn and D. Derauw, "Ice-dynamic conditions of Shirase Glacier, Antarctica, inferred from ERS SAR interferometry," *J. Glaciology*, vol. 48, no. 163, pp. 559–565, 2002.

[12] F. Casu, A. Manconi, A. Pepe, and R. Lanari, "Deformation time-series generation in areas characterized by large displacement dynamics: The SAR amplitude pixel-offset SBAS technique," *IEEE Trans. Geosci. Remote Sens.*, vol. 49, no. 7, pp. 2752–2763, Jul. 2011.

[13] D. Massonnet *et al.*, "The displacement field of the Landers earthquake mapped by radar interferometry," *Nature*, vol. 364, no. 6433, pp. 138–142, 1993.

[14] J. Mouginot, B. Scheuch, and E. Rignot, "Mapping of ice motion in Antarctica using synthetic-aperture radar data," *Remote Sens.*, vol. 4, no. 9, pp. 2753–2767, 2012.

[15] I. Joughin, B. E. Smith, and W. Abdalati, "Glaciological advances made with interferometric synthetic aperture radar," *J. Glaciology*, vol. 56, no. 200, pp. 1026–1042, Dec. 2010.

[16] R. Mottram *et al.*, "What is the surface mass balance of Antarctica? An intercomparison of regional climate model estimates," *Cryosphere Discuss.*, vol. 2020, pp. 1–42, 2020. [Online]. Available: https://www.the-cryosphere-discuss.net/tc-2019--333/

[17] J. Mouginot, E. Rignot, and B. Scheuchl, "Continent-wide, interferometric SAR phase, mapping of Antarctic ice velocity," *Geophys. Res. Lett.*, vol. 46, no. 16, pp. 9710–9718, 2019. [Online]. Available: https://agupubs.onlinelibrary.wiley.com/doi/abs/10.1029/2019GL083826

[18] L. Padman, M. King, D. Goring, H. Corr, and R. Coleman, "Ice-shelf elevation changes due to atmospheric pressure variations," *J. Glaciology*, vol. 49, no. 167, pp. 521–526, 2004.

[19] P. Dutrieux *et al.*, "Pine island glacier ice shelf melt distributed at kilometre scales," *Cryosphere*, vol. 7, no. 5, pp. 1543–1555, 2013. [Online]. Available: https://www.the-cryosphere.net/7/1543/2013/

[20] G. Moholdt, L. Padman, and H. A. Fricker, "Basal mass budget of ross and Filchner-Ronne ice shelves, Antarctica, derived from Lagrangian analysis of ICESat altimetry," *J. Geophys. Res., Earthq. Surf.*, vol. 119, no. 11, pp. 2361–2380, 2014. [Online]. Available: https://agupubs.onlinelibrary.wiley.com/doi/abs/10.1002/2014JF003171

[21] S. Berger, R. Drews, V. Helm, S. Sun, and F. Pattyn, "Detecting high spatial variability of ice shelf basal mass balance, Roi Baudouin ice shelf, Antarctica," *Cryosphere*, vol. 11, no. 6, pp. 2675–2690, 2017. [Online]. Available: https://www.the-cryosphere.net/11/2675/2017/

[22] M. A. King, T. Murray, and A. M. Smith, "Non-linear responses of Rutford ice stream, Antarctica, to semi-diurnal and diurnal tidal forcing," *J. Glaciology*, vol. 56, no. 195, pp. 167–176, 2010.

[23] S. H. Rosier, O. J. Marsh, W. Rack, G. H. Gudmundsson, C. T. Wild, and M. Ryan, "On the interpretation of ice-shelf flexure measurements," *J. Glaciology*, vol. 63, no. 241, pp. 783–791, 2017.

[24] W. Rack, M. A. King, O. J. Marsh, C. T. Wild, and D. Floricioiu, "Analysis of ice shelf flexure and its InSAR representation in the grounding zone of the southern McMurdo Ice Shelf," *Cryosphere*, vol. 11, no. 6, pp. 2481–2490, 2017.

[25] C. T. Wild, O. J. Marsh, and W. Rack, "Viscosity and elasticity: A model intercomparison of ice-shelf bending in an Antarctic grounding zone," *J. Glaciology*, vol. 63, no. 240, pp. 573–580, 2017.

[26] C. T. Wild, O. J. Marsh, and W. Rack, "Unraveling InSAR observed Antarctic ice-shelf flexure using 2-D elastic and viscoelastic modeling," *Frontiers Earth Sci.*, vol. 6, 2018, Art. no. 28. [Online]. Available: https://www.frontiersin.org/article/10.3389/feart.2018.00028

[27] M. Mcmillan *et al.*, "Mapping ice-shelf flow with interferometric synthetic aperture radar stacking," *J. Glaciology*, vol. 58, no. 208, pp. 265–277, 2012.

[28] H. Han and H. Lee, "Tide deflection of Campbell Glacier Tongue, Antarctica, analyzed by double-differential SAR interferometry and finite element method," *Remote Sens. Environ.*, vol. 141, pp. 201–213, 2014. [Online]. Available: http://dx.doi.org/10.1016/j.rse.2013.11.002

[29] H. Han and H. Lee, "Tide-corrected flow velocity and mass balance of Campbell Glacier Tongue, East Antarctica, derived from interferometric SAR," *Remote Sens. Environ.*, vol. 160, pp. 180–192, 2015. [Online]. Available: http://dx.doi.org/10.1016/j.rse.2015.01.014
[30] O. J. Marsh, W. Rack, D. Floricioiu, N. R. Golledge, and W. Lawson, "Tidally induced velocity variations of the beardmore glacier, Antarctica, and their representation in satellite measurements of ice velocity," *Cryosphere*, vol. 7, no. 5, pp. 1375–1384, 2013.
[31] M. Ruckamp, N. Neckel, S. Berger, A. Humbert, and V. Helm, "Calving induced speedup of Petermann Glacier," *J. Geophys. Res., Earthq. Surf.*, vol. 124, no. 1, pp. 216–228, 2019. [Online]. Available: https://agupubs.onlinelibrary.wiley.com/doi/abs/10.1029/2018JF004775
[32] G. Gomba, A. Parizzi, F. De Zan, M. Eineder, and R. Bamler, "Toward operational compensation of ionospheric effects in SAR interferograms: The split-spectrum method," *IEEE Trans. Geosci. Remote Sens.*, vol. 54, no. 3, pp. 1446–1461, Mar. 2016.
[33] G. H. Gudmundsson, "Tides and the flow of Rutford ice stream, West Antarctica," *J. Geophys. Res., Earthq. Surf.*, vol. 112, no. F4, 2007, Art. no. F04007. [Online]. Available: https://agupubs.onlinelibrary.wiley.com/doi/abs/10.1029/2006JF000731
[34] L. Padman, H. A. Fricker, R. Coleman, S. Howard, and L. Erofeeva, "A new tide model for the Antarctic ice shelves and seas," *Ann. Glaciology*, vol. 34, pp. 247–254, 2002.
[35] L. Padman, S. Y. Erofeeva, and H. A. Fricker, "Improving Antarctic tide models by assimilation of ICESat laser altimetry over ice shelves," *Geophys. Res. Lett.*, vol. 35, no. 22, 2008, Art. no. L22504. [Online]. Available: https://agupubs.onlinelibrary.wiley.com/doi/abs/10.1029/2008GL035592
[36] E. Rignot, J. Mouginot, and B. Scheuchl, "Antarctic grounding line mapping from differential satellite radar interferometry," *Geophys. Res. Lett.*, vol. 38, no. 10, 2011, Art. no. L10504. [Online]. Available: https://agupubs.onlinelibrary.wiley.com/doi/abs/10.1029/2011GL047109
[37] R. Drews, "Evolution of ice-shelf channels in Antarctic ice shelves," *Cryosphere*, vol. 9, no. 3, pp. 1169–1181, 2015.
[38] D. Callens, R. Drews, E. Witrant, M. Philippe, and F. Pattyn, "Temporally stable surface mass balance asymmetry across an ice rise derived from radar internal reflection horizons through inverse modeling," *J. Glaciology*, vol. 62, no. 233, pp. 525–534, 2016.
[39] S. Berger, L. Favier, R. Drews, J.-J. Derwael, and F. Pattyn, "The control of an uncharted pinning point on the flow of an Antarctic ice shelf," *J. Glaciology*, vol. 62, no. 231, p. 37–45, 2016.
[40] K. Matsuoka, A. Skoglund, and G. Roth, "Quantarctica," 2018. [Online]. Available: https://doi.org/10.21334/npolar.2018.8516e961
[41] H. Hersbach and D. Dee, "Era5 reanalysis is in production," *ECMWF Newslett.*, vol. 147, no. 7, pp. 5–6, 2016.

Quentin Glaude (Graduate Student Member, IEEE) received the master's degree in geomatics in 2017. He is currently working toward the Ph.D. degree in cograduation with the Universite Libre de Bruxelles (ULB) Brussels, Belgium, and the Universite de Liege (ULiege), Liège, Belgium. His Ph.D. thesis aims at improving the short-term monitoring of ice shelves using TOPSAR mode.

He is a Remote Sensing Specialist, especially in SAR remote sensing and TOPSAR interferometry. His research is supported by the French Community of Belgium in the funding context of a FRIA grant.

Charles Amory received the master's degree in environmental and earth sciences and the Ph.D. degree in Antarctic climate from the University Grenoble Alpes, Saint-Martin-d'Héres, France, in 2012 and 2016, respectively.

Since then has been a Postdoctoral Researcher with the FNRS, University of Liège, Liège, Belgium. His research interests include the climate system over the Antarctic and the Greenland ice sheets. He is mainly involved in the development and use of the regional climate model MAR designed to simulate climate specificities of polar regions and collection and analysis of meteorological data in polar environments, with a particular emphasis on drifting snow processes.

Sophie Berger received the Ph.D. degree in stability of Antarctic ice shelves from the Universite Libre de Bruxelles, Brussels, Belgium, in 2017.

She is currently a Postdoc with the Alfred Wegener Institut, Bremerhaven, Germany. She is working on various remote sensing data and techniques to investigate the dynamics and stability of the ice shelves in Dronning Maud Land (East Antarctica). She tweets as @SoBrgr.

Dominique Derauw received the M.Sc. degree in physics and the Ph.D. degree in sciences from the University of Liège, Liège, Belgium, in 1989 and 1999, respectively.

He is currently an Assistant Professor with the University of Rio Negro, General Roca, Argentina, a research fellow with the Ecole de Commerce et de Gestion, Luxembourg City, Luxembourg, and a Project Manager with the Signal Processing Lab, Centre Spatial de Liège, Liège, Belgium. His researches concentrate on SAR remote sensing and interferometric SAR applications and developments.

Frank Pattyn received the Ph.D. degree in sciences from the Vrije Universiteit Brussel, Brussels, Belgium, in 1998.

He is currently a Full Professor with the Université libre de Bruxelles, Brussels, Belgium. His research concentrates on Antarctic ice dynamics and ice sheet modeling. He is a President of the Belgian National Committee for Antarctic Research and the Associate Chief Editor of *Journal of Glaciology*.

Christian Barbier received the master's degree in physics mathematical physics and the Ph.D. degree in physics (unimolecular decay of electronically excited ions) from the University of Liège, Liège, Belgium, in 1980 and 1983, respectively.

He pursued a theoretical physicist career in the field of *ab initio* quantum mechanical calculation of linear and nonlinear optical properties of organic molecules and polymers. He entered Centre Spatial de Liège, in 1988 and began to be active in the field of SAR soon thereafter. Through ESA and Belgian government contract, he set up SAR image reconstruction and interferometry. He headed the Signal Processing Laboratory from 1989 to 2017. He also has teaching activities with the University of Liège with courses on theoretical cosmology, remote sensing, and space mission designs.

Anne Orban received the M.S. degree in physics in ionizing radiation and radioprotection from the Université Catholique de Louvain, Ottignies-Louvain-la-Neuve, Belgium, in 1987.

Since 1988, she has been with the Centre Spatial de Liège, Liège, Belgium, first in the Space Environment group, then in the Signal Processing Laboratory since 2017. Her main research interests are oriented toward remote sensing and earth observation, including SAR processing and InSAR, PolSAR, and PolInSAR applications.